

ARTICLE



Influence of expiratory flow pulsatility on the effectiveness of a surgical mask

Sarah Morris¹✉, William McAtee¹, Jesse Capecelatro² and Vrishank Raghav¹✉

© The Author(s), under exclusive licence to Springer Nature America, Inc. 2022

BACKGROUND: Expiratory events, such as coughs, are often pulsatile in nature and result in vortical flow structures that transport expiratory particles. The World Health Organization recommends wearing face masks to reduce the airborne transmission of diseases such as SARS-CoV-2 (COVID-19). However, masks are not perfect as flow leakage occurs around the mask, and their effectiveness under realistic (multi-pulse) coughing conditions is unknown.

OBJECTIVE: To assess the influence of expiratory flow pulsatility on the effectiveness of a surgical face mask by quantifying and classifying the flow leakage around the mask.

METHODS: A custom-built pulsatile expiratory flow simulator is used to generate single- and multi-pulsed coughing events. Flow visualization and particle image velocimetry are used to assess the penetration distance and volume of leakage flow at the top and sides of a surgical mask.

RESULTS: Leakage flow velocity profiles at the top and sides of a surgical mask take the form of a wall jet and a free-shear jet, respectively. Multi-pulsed expiratory flow events are found to generate greater leakage flow around the mask than single-pulsed events.

SIGNIFICANCE: For the first time, the leakage volume of a surgical mask is shown to be correlated to the pulsatile nature of a cough.

IMPACT STATEMENT: The novelties of this study are: First, flow field measurements are used to quantify and classify the leakage flow fields around the top and sides of a surgical mask, providing a benchmark for quantitative modeling of leakage flow velocity profiles. Second, the influence of pulsatility on the effectiveness of surgical face masks is studied by quantifying the leakage volume. For the first time, the leakage volume of a surgical mask is shown to be correlated to the pulsatile nature of a cough, as multi-pulsed expiratory flow events are found to generate greater flow leakage around the mask than single-pulsed events.

Keywords: COVID-19; Face masks; Coughing dynamics

Journal of Exposure Science & Environmental Epidemiology (2022) 32:697–705; <https://doi.org/10.1038/s41370-022-00416-x>

INTRODUCTION

It has been well established that diseases such as SARS-CoV-2 (COVID-19) are spread by airborne transmission, as respiratory expirations such as talking, coughing and sneezing produce small, virus-laden droplets [1, 2]. The airborne transmission of infectious particles is one of two primary methods for spreading infectious diseases (the other being Fomite transmission) [3]. The particles present in respiratory clouds generated by coughing are produced by the atomization of secretions that line the respiratory system as air travels from the lungs to the mouth, as well as the atomization of saliva at the mouth [4]. In particular, the particles present in respiratory clouds have been shown to originate in three primary locations: small droplets (<1–5 μm) originate via bronchiolar film rupture, 5–20 μm droplets via a laryngeal mode and droplets >50 μm in the oral cavity [5, 6]. It is the atomization of particles at the site of infection that causes droplets to contain infectious particles, and so the distribution of contagious particles in an expiratory

event is dependent on the site of infection. Significant research is still required into the dispersion of droplets via respiratory expirations, due to a lack of universal agreement as to particulate sizes [7]. Small particles of $\mathcal{O}(1 \mu\text{m})$ in the expiratory flow are quick to evaporate and aerosolize and these droplet nuclei remain suspended in continuum with the expiratory flow, becoming more buoyant as large particles fall from the cloud [8]. These small particles can stay airborne for hours, with the COVID-19 virus specifically having a half-life of more than an hour [9]. Furthermore, the extent of dispersion of these suspended aerosolized droplets depends on the fluid dynamics of the expiratory event and this has been previously studied both via experiment [10–12] and via computational fluid dynamics (CFD) [13, 14]. When an expiratory event such as a cough or sneeze occurs, the high-velocity flow from the mouth generates vortex ring structures [5, 15], with the size and strength of the vortex ring dependent on the expulsion process. As such, the human cough is

¹Auburn University, Department of Aerospace Engineering, Auburn, AL, USA. ²University of Michigan, Department of Mechanical Engineering, Ann Arbor, MI, USA.
✉email: sem0116@auburn.edu; raghav@auburn.edu

Received: 24 August 2021 Revised: 20 January 2022 Accepted: 24 January 2022
Published online: 7 February 2022

often modeled as an impulsively started jet. In particular, it can be characterized as a two-stage jet consisting of a starting-jet stage (SJS) and an interrupted-jet stage (IJS): the streamwise penetration distance of a cough in the SJS scales with $t^{1/2}$ and with $t^{1/4}$ in the IJS [12].

In actuality, however, the human cough is normally characterized as a multi-pulsed event, referred to as cough epochs, with each pulse lasting ~ 0.3 s [10, 12]. It has been shown that the flow rate profiles of these multi-pulsed events are the same as single-pulsed events, with subsequent pulses having lower amplitudes than the original pulse [10]. Furthermore, regular speech can form a train of pulsatile jets, as different speech patterns in succession will continually produce different strength jets [16]. In contrast to the single impulsively started jet, this multi-pulsed jet results in the formation of multiple viscous vortex rings [12, 17]. Entrainment considerably increases for pulsing jet flow [18], and the penetration distance of a pulsed jet has been shown to be greater than that of a steady jet [19]. The circulation motion of the generated vortex rings also serve to enhance the transport of the small airborne particles suspended within the flow field [17]. In the case of multi-pulsed events, the volume required for such expirations originates deeper in the lungs. As such, if the site of infection is also deep in the lungs (the site where very small droplets originate), then the pulsatile flow can also potentially expose more contagions to the environment [5].

To reduce the dispersion of infectious aerosol and transmission of airborne infectious diseases, the United States' Centers for Disease Control and Prevention (CDC) and the World Health Organization (WHO) recommend the use of face masks [20, 21]. The effectiveness of wearing a face mask to reduce disease transmission has been well established in literature [17, 22, 23]. In particular, it has been shown that particle (also referred to as droplet) dispersion in the original expiratory direction (i.e., directly through the mask) is significantly reduced [24, 25]. A number of studies have also investigated the filtration efficiency of masks under different conditions (see for example [26–28]). Whilst flow is reduced through the mask wall, studies have identified significant flow leakage at the side and top edges of masks (including N95, surgical, cloth, homemade). This leakage has been studied experimentally using smoke flow visualization [29–31], Schlieren imaging [32] and CFD [23].

To the authors' knowledge however, the leakage flow fields that are present at the side and top edges of surgical masks have not yet been comprehensively quantitatively measured. Furthermore, the influence of expiratory flow pulsatility on the effectiveness of masks is unknown. The amount of leakage from a face mask can be viewed as a function of both the fit of the mask on the face and the material properties of the mask [33, 34]. It is hypothesized that a pulsatile event could lead to more complex fluid-structure interactions with a mask than a single-pulsed event, thereby increasing the amount of flow leakage. To this end, this study aims to address an identified need for a quantitative experimental analysis of the flow leakage around face masks [33] by measuring the flow leakage around a commonly used surgical mask via particle image velocimetry (PIV). Quantification of this leakage gives a robust metric for evaluating mask performance to enhance mask design. Furthermore, such data on mask flow leakage can be used in risk-index modeling concerning disease spread, as well as in theoretical predictive models concerning disease spread (e.g., computational fluid dynamics (CFD)). These models will better enable public health and safety guidelines with respect to variables like air changeover rates for public indoor spaces.

This work therefore has a two-fold objective: (1) To quantify leakage flow fields around a surgical mask for the first time, and (2) To assess the influence of pulsatility on the leakage volume expelled around a surgical mask (i.e., the effectiveness of the mask). Three different flow rate conditions are considered in this

work to quantify the influence of multiple pulses on the dynamics of aerosol dispersion: a single-pulsed cough (S_1), a double-pulsed cough (D_1) wherein both pulses match S_1 , and a single-pulsed cough (S_2) wherein the area under the flow rate curve matches that of D_1 . A custom-built pulsatile expiratory flow simulator is used to generate the expiratory events, and flow visualization and particle image velocimetry are used to study the flow fields. In this study, the pulsatile expiratory flow simulator with no mask is first validated against literature. Quantitative flow field measurements are then used to identify and classify the leakage flow velocity profiles at the top and sides of a surgical mask. Lastly, the effect of pulsatility on the effectiveness of the surgical mask is examined by determining the leakage flow penetration distance and the normalized leakage volume expelled for each S_1 , D_1 and S_2 .

METHODS

Experimental setup

A custom-built pulsatile expiratory flow simulator (shown in Fig. 1a) in the Applied Fluids Research Group at Auburn University generates multi-pulsed coughing events. A computer-controlled solenoid valve (ASCO General Service Solenoid Valve, 8263H002, St. Louis, Missouri, USA) is used to provide the desired flow rates by controlling a pressurized air source at the wall. Since solenoid valves produce square-wave like flow rate profiles [35], an in-line pressure relief chamber is used to produce a more realistic (smoother) expiratory flow rate profile. An in-line gas flowmeter (Kelly Pneumatics Gas Flow Sensor, KPI-DMFS-1, Newport Beach, California, USA) is used to measure the flow rate at a sampling rate of 500 Hz, providing accurate mass flow rate readings. The outlet of the simulator is a pipe with length, $L = 121.9$ cm, and diameter, $D = 2.54$ cm, resulting in a pipe with $L/D \approx 48$. A mannequin face is placed at the end of the pipe with a corresponding 2.54 cm outlet to fit the pipe, allowing us to place the surgical mask on the mannequin's face. The mask used in this study is a commonly available surgical mask (Bigox 3-Ply non-medical). The surgical mask is a 17 cm \times 9.5 cm rectangle, as shown in Fig. 1b. This mask has a metal nose insert to fit the face, which is fit to the mannequin before each run. Elastic strings attach it around the mannequin's ears. A marker on the mannequin's nose is used as a guide to place the mask in the same location for each experiment. Furthermore, to test the sensitivity of the mask placement on the mannequin, the mask is placed at 1.27 cm (0.5D) and 2.54 cm (1D) below the base-line mask placement (see Fig. 1c). To prevent any ambient air currents from the room's ventilation system from interfering with the measured flow, all experiments were conducted in an ~ 3 m \times 3 m \times 3 m enclosure.

Flow conditions

To study the effects of pulsatility, three different flow conditions are tested in this study as illustrated in Fig. 1d: a single-pulsed cough (S_1), a double-pulsed cough (D_1) wherein both pulses match S_1 , and a single-pulsed cough (S_2) wherein the area under the flow rate curve (Cough Expired Volume (CEV)) matches that of D_1 . By controlling the pressure of the air source and the pulse width of the solenoid valve, the desired Cough Peak Flow Rates (CPFR) and pulsed flow rate durations are obtained. For single-pulsed coughs (S_1), this corresponds to a flow duration of $T_1 \approx 0.225$ s. The CPFR is ≈ 4.5 L/s; this is consistent with previously observed values in human coughing flow profiles [10]. It should be noted the CEV from the coughing simulator is expected to be higher than for a human cough. The single-pulse flow rate curve generated by the simulator is approximately symmetric, whereas the flow rate profile of a human cough has been previously approximated as a combination of gamma-probability-distribution functions, capturing the asymmetry of a human cough [10]. Similarly, the double-pulsed cough (D_1) flow rate is obtained by adjusting the control inputs; it must be noted that this generates two pulses of equal amplitude and duration; future studies will examine the effects of multi-pulsed events with decreasing amplitude to represent a more realistic human cough [10]. The three flow rate profiles (S_1 , D_1 , S_2) are repeated both with and without a mask, 3–5 times per experiment. The average standard deviation through the coughing event of these measured flow rate profiles is respectively: 0.12 LPS, 0.29 LPS and 0.15 LPS. For the mask placement sensitivity study (placement as shown in Fig. 1c), two additional experiments are conducted for the S_1 case referred to as S_{1a} and S_{1b} (each

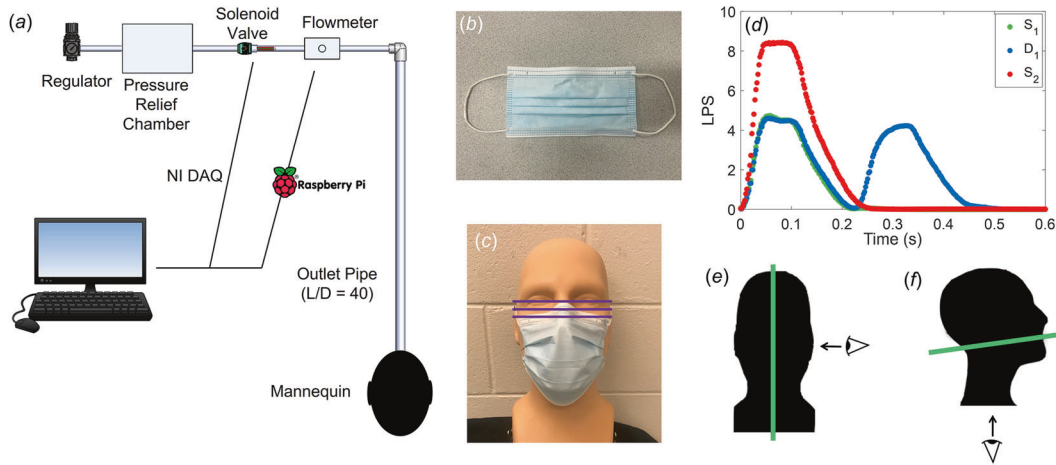


Fig. 1 Experimental setup of the pulsatile coughing simulator. **a** Computer-aided design schematic showing the main components of the coughing simulator; not to scale. **b** Surgical mask used in experiments. **c** Lines indicating the top-most mask location of the surgical mask on the mannequin's nose to study the sensitivity of mask placement. **d** Flow rate profile of an S_1 , D_1 and S_2 cough in litres per second (LPS). **e** Plane A intersects the middle of the mannequin's face, indicated in green. **f** Plane B intersects the mannequin's ear at $\sim 13^\circ$ to the horizontal, indicated in green.

of which were also repeated 3 times). The flow leakage around the mask is studied using two techniques, flow visualization and particle image velocimetry (PIV), which are discussed in the following sections.

Flow field assessment

Flow visualization. Flow visualization is initially used to examine the effect of pulsatility on the surgical mask configuration, both qualitatively and by measuring the flow penetration distance. Smoke generated by an Antari Z-800II Fog Machine (Taoyuan City, Taiwan) is used to visualize the flow. A luer-lock placed at the beginning (inlet) of the outlet pipe allows us to pre-fill the pipe with smoke for each experiment such that it is expelled during the expiratory event. The luer-lock is closed after filling and remains closed for each coughing event. A Nikon Z50 mirrorless camera is used to image the flow at 11 fps. A variable focal length lens was used with an exposure time of $1/1250$ seconds at an aperture of $f/1.8$. The exposure time was chosen to minimize any blurring in the images. Flow visualization images are taken in Plane A and Plane B as defined in Fig. 1e, f. Surgical mask images taken in Plane A are taken with a focal length of 18 mm and Plane B with a focal length of 24 mm. No mask images in Plane A are also taken with a focal length of 24 mm. These planes are illuminated using a Laserglow Technologies 532 nm continuous laser (Toronto, Canada); the laser beam is converted to a light sheet via two cylindrical lenses.

Particle image velocimetry. Planar PIV is used to obtain quantitative measurements of the flow in Plane A and Plane B, both with and without a mask. Prior to experiments, the tent is seeded with smoke particles (Antari Z-800II Fog Machine, mean diameter $2 \mu\text{m}$) and the pipe is also pre-filled with smoke, ensuring uniform particle seeding in the field of view through the entire expiratory event. A high-speed Photonics dual-head Nd:YLF pulsed-laser DM30-527 (Ronkonkoma, New York, USA) operating at 18 mJ/pulse at 250 Hz combined with a laser arm and light sheet generating optics (Intelligent Laser Applications GmbH, Jülich, Germany) is used to illuminate our field of view.

A Vision Research Phantom VEO 4K 990L high-speed camera (Vision Research Inc., Wayne, New Jersey, USA) is used to record particle motions. A Nikon AF variable focal length lens was used at a focal length of 50 mm for Plane A experiments and 18 mm for Plane B experiments. Image pairs were recorded at 250 Hz and at a resolution of 4096×2304 pixels, with $\delta T = 2000 \mu\text{s}$ between images for S_1 and D_1 , and $\delta T = 1250 \mu\text{s}$ for S_2 . The commercially available Davis10 software (LaVision GmbH, Göttingen, Germany) was used both to record the image pairs, and to process the images using cross-correlation based PIV. The interrogation window underwent 4 multi-passes with a final window size of 32×32 pixels and 75% window overlap to produce 2-dimensional, 2-component (2D-2C) vector fields; this resulted in a final vector spacing of 1.5 mm.

Data analysis

To calculate the penetration distance of the flow (no mask, and leakage flows in Plane A and Plane B), flow visualization images (such as Fig. 2a, c) are initially converted to a binary image in MATLAB. The dimensionless penetration distance is measured along the jet axis and is taken as the farthest point along the jet axis within a moving search window. For no mask, the jet axis is horizontal (parallel to x , as shown in Fig. 2a) and the dimensionless penetration distance is defined as x_D/D where x_D is the penetration distance along the jet axis. For Plane A and B, the leakage flow jet axis will be at an angle to the x - y or x - z axis, and the dimensionless penetration distance is defined as $x_{D,\text{jet},i}/D$, where i indicates Plane 'A' or 'B'. These rotated axes are $x_{\text{jet},A} - y_{\text{jet},A}$, and $x_{\text{jet},B} - z_{\text{jet},B}$ respectively. The rotated axes for Plane A and Plane B can be found in the Results and Discussion. When calculating the penetration distance, 3–5 runs of each case are taken and averaged. In each case (no mask, Plane A top mask leakage, Plane B side mask leakage), the scaling laws were fit using $At^n + c$ in both the starting jet stage and interrupted jet stage, where A and c are constants to fit the scaling laws, n is the known exponential for the starting jet and interrupted jet stages, and t is time.

Using the resultant velocity field from PIV, the finite-time Lyapunov Exponent (FTLE) is computed using the LCS MATLAB Kit Version 2.3 by the Biological Propulsion Laboratory at the California Institute of Technology [36–38]. The FTLE is useful in analyzing time-dependent velocity fields, as ridges in the FTLE field are used to define Lagrangian Coherent Structures (LCS) [36, 39]. The FTLE $\sigma_t^{t+T}(\mathbf{x})$ is given by:

$$\sigma_t^T(\mathbf{x}) = \frac{1}{|T|} \ln \left\| \frac{d\phi_t^{t+T}(\mathbf{x})}{d\mathbf{x}} \right\| \quad (1)$$

where ϕ_t^{t+T} denotes the flow map of particles from their location \mathbf{x} at time t to $t+T$. For full details see Shadden et al. [36]. For $T < 0$, the LCS can be referred to as a 'backward-time' LCS (bLCS): this is an attracting LCS, wherein the trajectory of fluid particles converge towards the LCS [40]. Similarly, for $T > 0$, the LCS is a 'forward-time' or repelling LCS (fLCS). LCS material lines are also transport barriers. In this study, we use the bLCS to show attracting material lines in the flow field, as a means of demonstrating where particles in the flow are likely to accumulate. The integration length of an LCS $|T|$ is somewhat arbitrary [36], and is generally taken as long as it takes to reveal the LCS. In this study, we use an integration length of 50 frames or $|T| = 0.2$ s.

To quantify the effectiveness of the surgical mask, the flow leakage velocity profile and normalized leakage volume are determined. To classify the leakage velocity profile, a line is taken perpendicular to the leakage flow axis. For no mask, the flow leakage axis is along the x axis. As aforementioned, for Plane A and Plane B a 2D transformation matrix is applied to the data such that the x axis aligns parallel with the leakage jet axis ($x_{\text{jet},i}$). The volume of leakage flow per unit span ($V_{l,\text{span}}$) is computed

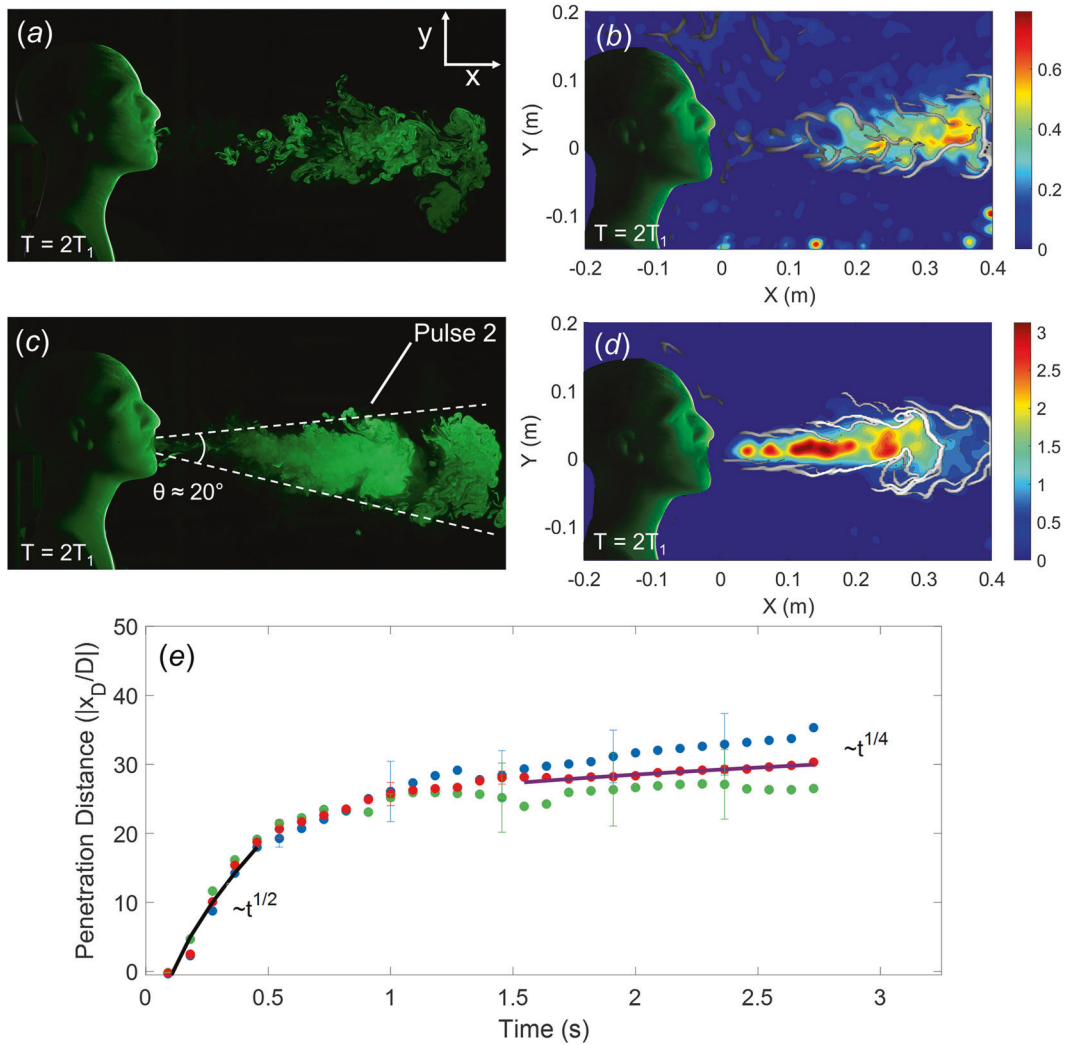


Fig. 2 Flow field results for coughing with no mask. **a** Flow visualization of a single-pulse cough, S_1 . **b** u velocity contours (m/s) of a single-pulse cough, S_1 , overlaid with bLCS contours. **c** Flow visualization of a double-pulse cough, D_1 , showing the second pulse. **d** u velocity contours of a double-pulse cough, D_1 , overlaid with LCS contours. The second pulse is visible, bounded by the LCS contour. **e** Streamwise penetration distance x_p/D for S_1 , D_1 and S_2 . The penetration distance scales with $t^{1/2}$ in the starting jet stage, and $t^{1/4}$ in the interrupted jet stage. Error bars based on the measurement standard deviation are shown on each curve.

along a line perpendicular to the leakage flow axis in both planes and is given by:

$$V_{l,span|A} = \int_0^T \int_{y_1}^{y_2} u_{jet,A}(y_{jet,A}) dy_{jet,A} dt \quad V_{l,span|B} = \int_0^T \int_{z_1}^{z_2} u_{jet,B}(z_{jet,B}) dz_{jet,B} dt \quad (2)$$

where $u_{jet,i}$ is first integrated over the distance over which the leakage velocity flow profile covers (i.e., y_1 and y_2 are the bounds of the leakage jet flow profile along the $y_{jet,A}$ axis and similar for $z_{jet,B}$), and these values are then integrated over time for the duration of the pulse(s) ($t = 0$ to $t = T$).

To enable a comparison across different cases, we normalize the leakage volume per unit span by the CEV per unit span (CEV/D), where CEV is determined from the mass flow rate curves shown in Fig. 1d, and is given by:

$$V_{leakage|A} = \frac{\int_0^T \int_{y_1}^{y_2} u_{jet,A}(y_{jet,A}) dy_{jet,A} dt}{\frac{CEV}{D}} \quad V_{leakage|B} = \frac{\int_0^T \int_{z_1}^{z_2} u_{jet,B}(z_{jet,B}) dz_{jet,B} dt}{\frac{CEV}{D}} \quad (3)$$

It is noted that care should be taken when interpreting this data not to extrapolate this volume leakage per unit span to a volumetric leakage flow, as the definition of $V_{leakage}$ is based on planar measurements.

RESULTS AND DISCUSSION

First, the pulsatile expiratory flow simulator without a mask is validated against existing literature. Second, the leakage flow that occurs at the top and sides of the surgical mask is quantified and classified. Last, the influence of coughing pulsatility on the effectiveness of the surgical mask is assessed both by quantifying the penetration distance and by estimating normalized leakage volume of the leakage flows.

Validation of pulsatile expiratory flow simulator

The simulator was validated using three benchmarks: the CPFR of S_1 , the spread angle of D_1 , and the streamwise penetration distance of each S_1 , D_1 and S_2 . As shown in Fig. 1d, the flow rate profile of the S_1 cough reaches a peak of ~ 4.5 L/s which is within the reported CPFR range of measured female and male coughs [10]. Figure 2 shows the flow visualization and PIV results of an S_1 ((a) and (b)) and a D_1 ((c) and (d)) cough at $T = 2T_1$. At this time, the difference in flow features between the two events is apparent. The vortex ring that is generated via the second pulse in D_1 is seen both in the smoke flow visualization (Fig. 2c) and in the u velocity contour plot via the bLCS field (Fig. 2d). High values

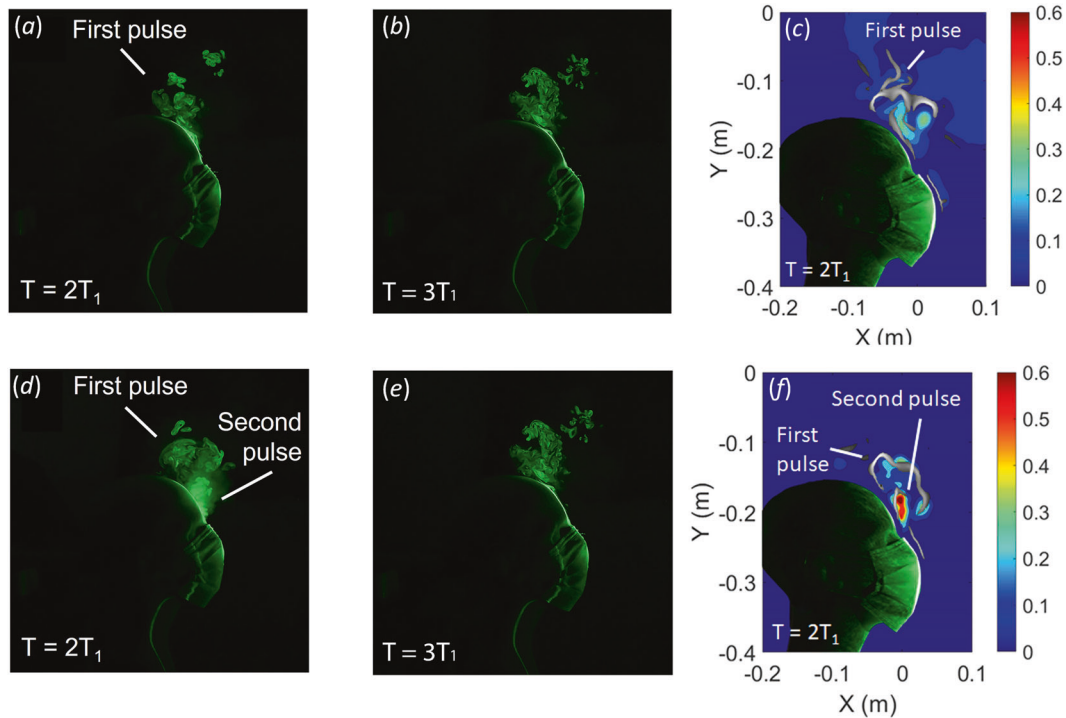


Fig. 3 Flow visualization and PIV results for Plane A. **a, b** Flow visualization of an S_1 cough in Plane A (see Fig. 1e for Plane A orientation). **c** u_{total} (m/s) velocity contour plot of an S_1 cough, overlaid with bLCS contours. **c, d** Flow visualization of a D_1 cough. **c** u_{total} (m/s) velocity contour plot of a D_1 cough, overlaid with bLCS contours.

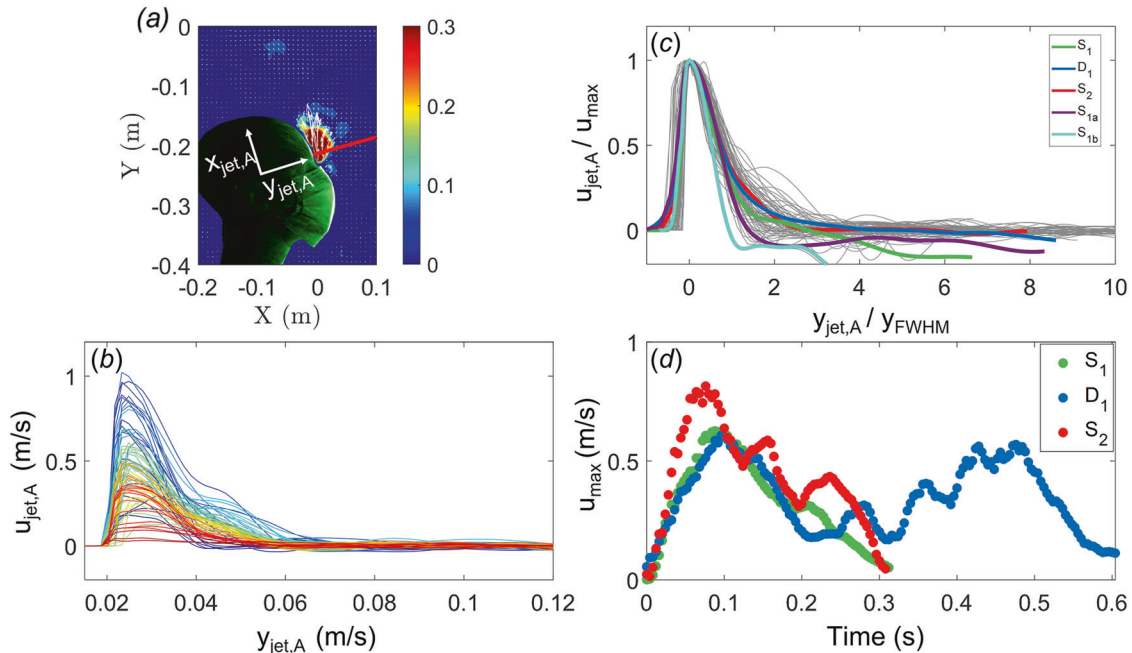


Fig. 4 Leakage jet characteristics at the top of the mask in Plane A. **a** u_{total} (m/s) velocity contour plot, showing 'line A' in red along which the leakage flow velocity profile is taken. The rotated axes $x_{\text{jet,A}}$ and $y_{\text{jet,A}}$ are indicated. **b** Leakage velocity flow profile for S_2 at line A. The time evolution is indicated by color, where increasing time ($\Delta t = 0.004$ s) goes from cool to warm. **c** Normalized leakage velocity flow profile. The gray lines show the normalized S_2 data from **b**, and the average normalized data is shown for each S_1 , D_1 , S_2 , S_{1a} and S_{1b} . **d** Maximum velocity attained along line A for S_1 , D_1 and S_2 . The data has been smoothed using a 10-point moving average.

of a bLCS contour indicate regions of high particle attraction; as such, small airborne particles will be expected to follow these boundaries. As LCS structures are barriers to material transport, Fig. 2d indicates that a boundary between the first and second

vortex rings exist in the D_1 flow field at this time point. This is consistent with previous computational results of multi-pulsed particle-laden coughs, wherein the distribution of particles originating from separate pulses initially remain separate, prior

to mixing at late times [5]. Figure 2c also shows the spread angle of the double-pulsed cough at $T = 2T_1$, measured to be $\approx 20^\circ$ from flow visualization. This is consistent with past studies, wherein the spread angle has been reported as 20.8° [12] and 23.9° [32].

The non-dimensional streamwise penetration distances x_D/D for S_1 , D_1 and S_2 were measured via flow visualization. Past studies have characterized coughing flows as a two-stage jet, wherein the starting-jet stage (SJS) and interrupted-jet stage (IJS) are two distinct phases of flow. In the SJS, the temporal growth scales with $t^{1/2}$; this phase is dominated by jet-like dynamics. In the IJS, the temporal growth scales with $t^{1/4}$ and is dominated by puff-like dynamics, as the source is no longer delivering momentum to the flow [8, 12, 41]. The temporal growth in the IJS is therefore slower than in the SJS. These scaling laws are found to fit well with the no mask data, as shown in Fig. 2e.

Identification and classification of leakage flow around a surgical mask

Top leakage (Plane A). The first area of flow leakage that was examined was the top of the surgical mask. As is shown in Fig. 1e, the top leakage is measured in the plane down the middle of the mannequin's face (Plane A). The flow leakage is shown via flow visualization and PIV for both an S_1 (Fig. 3a–c) and D_1 (Fig. 3d–f) cough. The time period is defined after the flow begins leaking from the top of the mask. It is interesting to note in the flow visualization (Fig. 3a, b, d, e) that the top flow leakage does not travel directly vertically upward. Rather, the flow stays by the mannequin head (even beyond the images presented in Fig. 3). As will be discussed below, this results in a wall jet along the mannequin's forehead. Figure 3c, f show the total velocity contour plot, $u_{\text{total}} = (u^2 + v^2)^{1/2}$, overlaid with bLCS contours for cough S_1 and D_1 respectively. The bLCS contours indicate that particles are expected to concentrate towards the plume front of both the S_1 and D_1 ; a bLCS contour beginning to form around the second pulse of D_1 is also observed, indicating a second plume front of particle accumulation.

The top flow leakage velocity profile acquired in Plane A is taken perpendicular to the leakage flow axis ('line A'), set at an angle θ to the x-y plane as shown in Fig. 4a, where the $x_{\text{jet,A}}$ axis aligns with the jet flow axis. At the top of the surgical mask the flow leakage velocity profile takes the form of a wall jet, which forms along the mannequin's forehead. This was observed in each of the S_1 , D_1 and S_2 cases. The leakage velocity profile $u_{\text{jet,A}}$ is shown for S_2 in Fig. 4b, wherein the time evolution of the wall jet at line A progresses from cool to warm colors. The wall jet that

forms is self-similar and scales with the maximum velocity u_{max} and the full width at half maximum y_{FWHM} of the jet. This is shown in Fig. 4c. The normalized S_2 data is shown in gray: the y-axis is normalized as $u_{\text{jet,A}}/u_{\text{max}}$ and the x-axis is normalized by $y_{\text{jet,A}}/y_{\text{FWHM}}$. The maximum velocity ($u_{\text{jet,A}}/u_{\text{max}} = 1$) is centered over $y_{\text{jet,A}}/y_{\text{FWHM}} = 0$. The average normalized velocity profiles (shown in Fig. 4c) agree well with each other for all cases, only deviating as they move further away from the wall jet center-line ($y_{\text{jet,A}}/y_{\text{FWHM}} > 3$) when the velocity is low and the magnitude of $v_{\text{jet,A}}$ was observed to approach $u_{\text{jet,A}}$.

In addition to the base-line S_1 case, two additional S_1 cases were run to test the sensitivity of different mask placements (S_{1a} and S_{1b}). These are defined in Experimental Setup and shown in Fig. 1c. The average normalized leakage flow velocity profiles for S_{1a} (purple) and S_{1b} (cyan) match reasonably well with the baseline cases taken at the topmost location on the mannequin's nose. This indicates that even when the mask placement is placed 0.5D and 1D further down the nose, a self-similar wall jet is still formed along line A. The flow leakage velocity profile is therefore relatively robust to mask placement (assuming it is placed along the nose, as recommended by the WHO and CDC), and can be modeled as a wall jet. This also indicates the robustness of our chosen line A: the flow leakage velocity profile can be taken at different locations above the top of the surgical mask and will still return the same normalized wall jet. Figure 4d shows the time progression of the maximum velocity along line A, taken from when the flow begins leaking from the top of the mask. Two main features are observed. The first pulse of D_1 and S_1 closely follow each other, as is expected. However, the maximum velocity of S_2 compared to S_1 and D_1 does not proportionally scale with the CPFR of S_2 compared to S_1 and D_1 . This suggests that the surgical mask has better attenuated the cough with higher CPFR.

Side leakage (Plane B). The second area of flow leakage identified is at the sides of the surgical mask in Plane B. As is shown in Fig. 1f, this plane is taken at $\sim 13^\circ$ to the horizontal. This plane was chosen as it was observed to follow the flow leakage axis at the side. The leakage flow is shown in Fig. 5 via flow visualization and PIV; the image is viewing up at the inclined plane as indicated in Fig. 1f. Figure 5a, b show an S_1 cough; Fig. 5c, d show a D_1 cough. Each frame is shown at a time period of $2T_1$ after the flow begins leaking from the side of the mask. At this time, the second pulse of the D_1 cough is clearly visible in the smoke flow visualization when compared to S_1 . To quantitatively examine this difference,

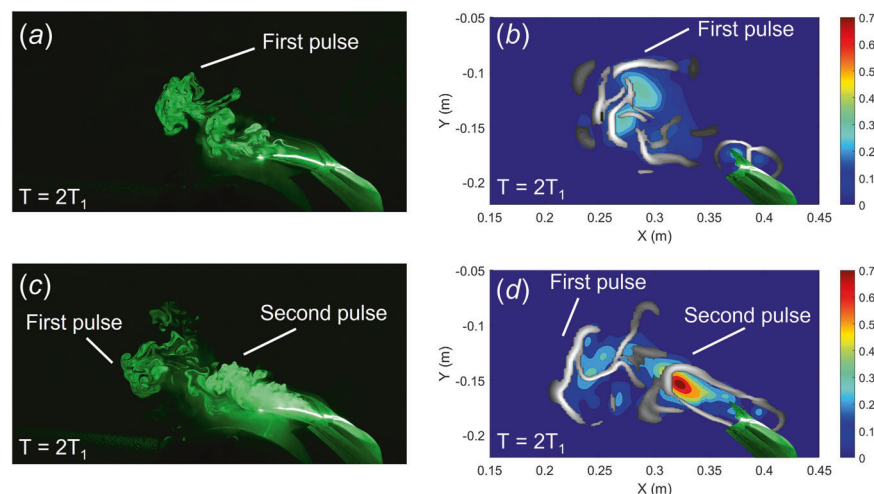


Fig. 5 Flow visualization and PIV results for Plane B. **a** Flow visualization of an S_1 cough in Plane B (see Fig. 1f for Plane B orientation). **b** u_{total} (m/s) velocity contour plot of an S_1 cough, overlaid with bLCS contours. **c** Flow visualization of a D_1 cough. **d** u_{total} (m/s) velocity contour plot of a D_1 cough, overlaid with bLCS contours. The second pulse of the D_1 cough is clearly seen in both flow visualization and PIV.

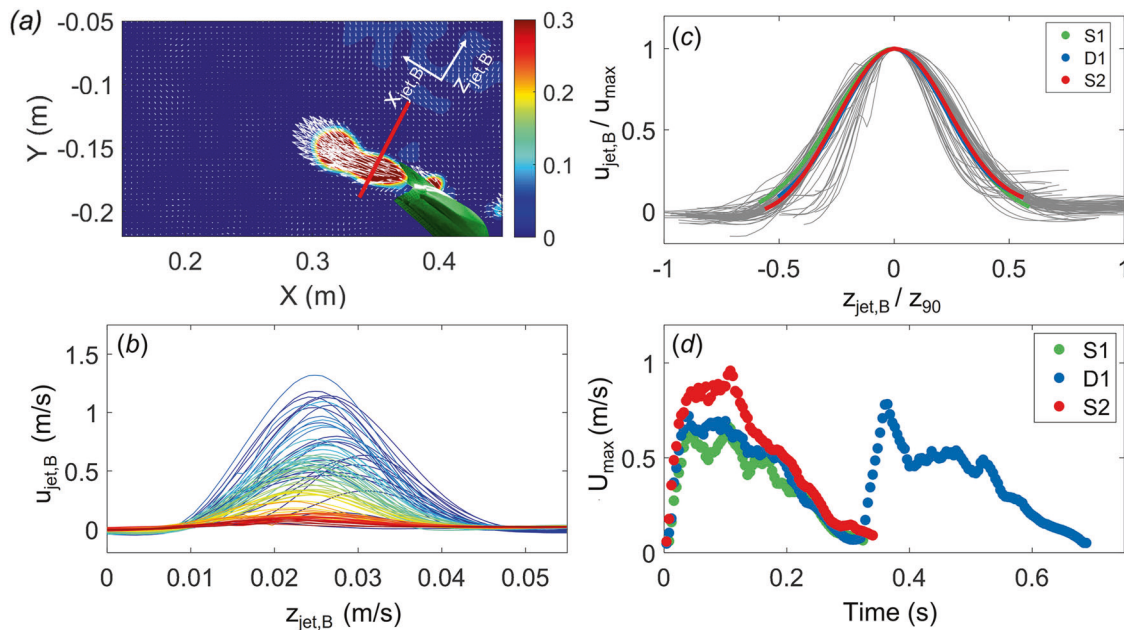


Fig. 6 Leakage jet characteristics at the side of the mask in Plane B. **a** u_{total} (m/s) velocity contour plot, showing 'line B' in red along which the leakage flow velocity profile is taken. The rotated axes $x_{jet,B}$ and $z_{jet,B}$ are indicated. **b** Leakage velocity flow profile for S_2 at line B. The time evolution is indicated by color, where increasing time ($\Delta t = 0.004$ s) goes from cool to warm. **c** Normalized leakage velocity flow profile. The gray lines show the normalized S_2 data from **b**, and the average normalized data is shown for each S_1 , D_1 and S_2 . **d** Maximum velocity attained along line B for S_1 , D_1 and S_2 . The data has been smoothed using a 10-point moving average.

the total velocity contour plot is shown, u_{total} , with bLCS contours overlaid on top. The bLCS contours indicate that particles are expected to concentrate towards the plume front of the first pulse in both S_1 and D_1 , and also at the plume front of the second pulse for D_1 . This is consistent with previous observations [16], wherein rakes of particles implemented at an expiratory source were seen to accumulate at the plume front. This indicates that the plume front will contain a higher concentration of particles than the tail, as small aerosols that stay suspended in the respiratory cloud will conglomerate near the front. In the case of a double-pulsed cough, the tail may contain particles for longer than a single-pulsed cough, as the particle-containing second plume front propagates forward.

To classify the flow leakage velocity profile at the side of the mask, a line was taken ~ 5 cm from the edge of the mask, perpendicular to the leakage jet axis ('line B') at an angle θ to the x - z plane. The rotated axis is shown in Fig. 6a. In contrast to Plane A, the flow leakage profile at the side of the surgical mask takes the form of a free-shear jet. This was observed in each S_1 , D_1 and S_2 . The leakage velocity profile $u_{jet,B}$ is shown for S_2 in Fig. 6b, where the time evolution of the free-shear jet at line B progresses from cool to warm colors. As illustrated in Fig. 6c, the jet that forms is self-similar and scales with the maximum velocity u_{max} and the width of the jet when $u_{jet,B} = 0.1 u_{max}$ (referred to as z_{90}). The normalized S_2 data is shown in gray: the y -axis is normalized as $u_{jet,B}/u_{max}$ and the x -axis is normalized by $z_{jet,B}/z_{90}$ and adjusted to align the peaks. All three cases take the form of a free-shear jet, and are self-similar when scaled by u_{max} and z_{90} .

Figure 6d shows the time progression of the maximum velocity along line B, taken from when the flow begins leaking from the side of the mask. Similarly to the top flow leakage in Plane A, the first pulse of D_1 and S_1 closely follow each other. Once again, the maximum velocity of S_2 compared to S_1 and D_1 does not proportionally scale with the CPFR of S_2 compared to S_1 and D_1 . An additional observation is that the second pulse of D_1 reaches a higher maximum velocity and persists for a longer duration than the first pulse (≈ 0.4 s compared to ≈ 0.3 s). It is possible that the

first pulse dislodges or reduces the 'quality of fit' of the mask such that more expiratory flow escapes during subsequent pulses.

Effect of pulsatility on leakage around a surgical mask

To assess the effect of pulsatility on the effectiveness of a surgical mask, the penetration distance and normalized leakage volume of the leakage flow expelled at the top of the mask in Plane A and at the side of the mask in Plane B are quantified. The penetration distance along the leakage jet axis, $x_{Djet,i}/D$, is shown in Fig. 7 for (a) the top leakage in Plane A and (c) for the side leakage in Plane B, taken from when the flow begins leaking from the side of the mask. Three key features are observed. Firstly, in both Plane A and Plane B the penetration distance scale with the same trends as for the no mask case. In the SJS jet-like dynamics dominate, and the temporal growth scales with $t^{1/2}$. In the IJS puff-like dynamics dominate, and the temporal growth scales with $t^{1/4}$. Secondly, it is also observed that for the top leakage in Plane A, the double-pulsed cough has a larger penetration distance than either of the single-pulsed coughs: D_1 is $\approx 20\%$ further than S_1 after 2.5 s. In contrast, all three cases are comparable in the Plane B side leakage; the D_1 cough only appears to be overtaking S_2 at later times. Lastly, it is interesting to compare the non-dimensional penetration distances to the no-mask case. In the no mask case, the penetration distance of D_1 was $x_D/D \approx 33$ at 2.5 s (for S_1 , $x_D/D \approx 26$). At the same time after beginning leakage from the mask (2.5 s), the D_1 cough has reached 54% of its no mask penetration distance in the Plane A top leakage and 56% in the Plane B side leakage; similarly, the S_1 cough has reached 56% of its no mask penetration distance in the Plane A top leakage and 72% in the Plane B side leakage.

The normalized volume of leakage flow (per unit input CEV, computed from Eq. (2)) along line A and line B (top and side of the surgical mask, respectively) is shown in Fig. 7b d, respectively. Two main features are observed. Firstly, at both the top and side leakage locations the double-pulsed cough contains more leakage volume expelled than either of the single-pulsed coughs (at least 40% greater than either single-pulsed cough's top flow leakage in

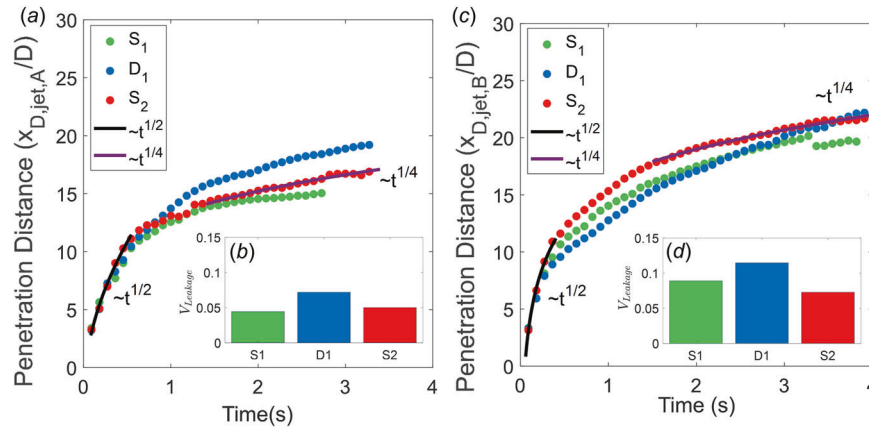


Fig. 7 Flow leakage quantification at the top and sides of the surgical mask. a Plane A top flow leakage penetration distance along the wall jet axis $x_{D_{jet,A}}/D$ for S_1 , D_1 and S_2 . **b** Normalized leakage volume expelled at the top of the mask in Plane A. **c** Plane B side flow leakage penetration distance along the jet axis $x_{D_{jet,B}}/D$ for S_1 , D_1 and S_2 . **d** Normalized leakage volume expelled at the side of the mask in Plane B.

Plane A, and at least 30% greater than either single-pulsed cough's side flow leakage in Plane B). This indicates that the pulsatile nature of the cough leads to a decrease in the effectiveness of the surgical mask. Previous studies have shown that perimeter leakage is primarily observed when a mask is loose and does not make a seal with the face [34, 42]. It is therefore possible that the first pulse of a multi-pulsed cough pre-loosens or reduces the 'quality of fit' of the mask (due to the increase in pressure inside the mask during a coughing event [23, 34]) before the second pulse, such that the effectiveness of the mask is reduced during subsequent pulses.

The second observation is that the leakage volume is at least 60% greater in the Plane B side flow leakage for each of S_1 , D_1 and S_2 than it is for the Plane A top flow leakage. This is consistent with previous qualitative Schlieren experiments that observed that the sides of a surgical mask allow more air leakage than the top [32]. This naturally follows by examining the leakage flow velocity profiles (Figs. 4 and 6) and the associated definition of leakage volume (Eq. (2)). Since the width of the leakage jet at the side of the mask (between the mask and cheek) is greater than that at the top of the mask (between the nose and mask), the side leakage volume is larger. The wider side leakage jet is most likely a result of the distribution of elastic forces of the surgical mask over the face. The top of the mask has two advantages compared to the side. Firstly, the elastic forces (stretching [34]) at the sides of the mask are along the surface of the face, inherently not providing as tight a seal as compared to over the nose. Secondly, the top of the mask includes a metal nose insert that has been shown previously to reduce top flow leakage [34]. When worn correctly, this metal nose insert conforms to the shape of the mannequin's nose. As the metal nose insert is more resistant to deformations than the material of the mask, it will continue to conform to the nose shape during expiratory events. In contrast, the flexible cloth at the side of the mask will be more susceptible to deformations, resulting in larger gaps between the cheek and mask.

Limitations

In this study, buoyancy and thermodynamics effects are not included as they are expected to have a minimal effect on the surgical mask leakage flow, as it is predominantly momentum-driven. As a mannequin was used in this study, a limitation that arose was the lack of hair and clothing features (e.g., long hair, beards, hats) that could change the leakage velocity flow profiles. Additionally, these results were all attained using a mannequin with a hard plastic face. It is possible that a soft (e.g., silicone or human skin) surface could lead to different leakage characteristics.

However, as both types of surfaces (hard or soft) provide a non-permeable and no-slip boundary condition to the flow, the leakage flow profiles found in this study are expected to remain at least qualitatively similar. Other masks were not studied in this work as there was no robust measure of mask fit, and reporting data from different mask configurations could give rise to unfair implications with respect to performance. It must also be noted that this work was limited to double-pulsed coughs of equal amplitude, rather than decaying in amplitude.

CONCLUSION

In this work, three coughing conditions are studied: a single-pulse (S_1), a double-pulse (D_1) consisting of two pulses the same as S_1 , and a single-pulse (S_2) with the same CEV as D_1 . The leakage flow velocity profiles at the top and sides of a surgical mask are found to take the form of a wall jet and a free-shear jet, respectively, for all cases. It was also observed that the leakage flow velocity profile was insensitive to mask placement. Multi-pulsed expiratory flow events are found to generate greater leakage flow around the mask than similar single-pulsed events. It is believed that the first pulse of a multi-pulsed event leads to fluid-structure interactions that increase the pressure inside the mask, pre-loosening and reducing the 'quality of fit' of the mask before subsequent pulse (s). The leakage volume was also greater at the sides of the mask than the top of the mask across all studied cases. Knowledge of mask leakage rates can be used to improve theoretical predictive models of indoor disease transmission, leading to optimization in mitigation strategies such as air changeover rates and physical distancing. Future studies will quantify mask fit in order to accurately compare the flow dynamics and flow leakage between different masks, such as a surgical and a cloth mask.

DATA AVAILABILITY

The datasets generated during and/or analyzed are available from the corresponding authors upon reasonable request.

REFERENCES

- Zhang R, Li Y, Zhang AL, Wang Y, Molina MJ. Identifying airborne transmission as the dominant route for the spread of COVID-19. *PNAS*. 2020;117:14857–63.
- Scharfman BE, Techet AH, Bush JWM, Bourouiba L. Visualization of sneeze ejecta: steps of fluid fragmentation leading to respiratory droplets. *Exp Fluids*. 2016;57:24.
- Wells WF. On air-born infection. Study II. droplet droplet. *Nucl Am J Hyg*. 1934;20:611–8.
- Hare RH. The transmission of respiratory infections. *Proc R Soc Med*. 1964;57:221–30.

5. Monroe K, Yao Y, Lattanzi A, Raghav V, Capeceaturo J. Role of pulsatility on particle dispersion in expiratory flows. *Phys Fluids*. 2021;33:043311.
6. Wei J, Li Y. Airborne spread of infectious agents in the indoor environment. *Am J Infect Control*. 2016;44:S102–S108. (9, Supplement)
7. Rosti ME, Olivieri S, Cavaiola M, Seminara A, Mazzino A. Fluid dynamics of COVID-19 airborne infection suggests urgent data for a scientific design of social distancing. *Sci Rep*. 2020;10:22426.
8. Bourouiba L, Dehandschoewercker E, Bush JWM. Violent expiratory events: on coughing and sneezing. *J Fluid Mech*. 2014;745:537–63.
9. van Doremalen N, Bushmaker T, Morris DH, Holbrook MG, Gamble A, Williamson BN, et al. Aerosol and surface stability of SARS-CoV-2 as compared with SARS-CoV-1. *N Engl J Med*. 2020;382:1564–7.
10. Gupta JK, Lin CH, Chen Q. Flow dynamics and characterization of a cough. *Indoor Air*. 2009;19:517–25.
11. Vansciver M, Miller S, Hertzberg J. Particle image velocimetry of human cough. *Aerosol Sci Technol*. 2011;45:415–22.
12. Wei J, Li Y. Human cough as a two-stage jet and its role in particle transport. *PLoS One*. 2017;12:e0169235.
13. Aliabadi AA, Rogak S, Green S, Bartlett K. CFD simulation of human coughs and sneezes: a study in droplet dispersion, heat, and mass transfer. *7*; 2010.
14. Dbouk T, Drikakis D. On coughing and airborne droplet transmission to humans. *Phys Fluids*. 2020;32:053310.
15. Akagi F, Haraga I, Inage SI, Akiyoshi K. Effect of sneezing on the flow around a face shield. *Phys Fluids*. 2020;32:127105.
16. Tan ZP, Silwal L, Bhatt SP, Raghav V. Experimental characterization of speech aerosol dispersion dynamics. *Sci Rep*. 2021;11:3953.
17. Simha PP, Rao PSM. Universal trends in human cough airflows at large distances. *Phys Fluids*. 2020;32:081905.
18. Vermeulen PJ, Ramesh V, Yu WK. Measurements of entrainment by acoustically pulsed axisymmetric air jets. *J Eng Gas Turbines Power*. 1986;108:479–84.
19. Johari H. Scaling of fully pulsed jets in crossflow. *AIAA J*. 2006;44:2719–25.
20. CDC. Improve How Your Mask Protects You. Centers for Disease Control and Prevention; 2021. <https://www.cdc.gov/coronavirus/2019-ncov/your-health/effective-masks.html>.
21. WHO. Coronavirus disease (COVID-19) advice for the public: when and how to use masks. World Health Organization; 2020. <https://www.who.int/emergencies/diseases/novel-coronavirus-2019/advice-for-public/when-and-how-to-use-masks>.
22. Akhtar J, Garcia AL, Saenz L, Kuravi S, Shu F, Kota K. Can face masks offer protection from airborne sneeze and cough droplets in close-up, face-to-face human interactions?—A quantitative study. *Phys Fluids*. 2020;32:127112.
23. Dbouk T, Drikakis D. On respiratory droplets and face masks. *Phys Fluids*. 2020;32:063303.
24. Aydin O, Emon B, Cheng S, Hong L, Chamorro LP, Saif MTA. Performance of fabrics for home-made masks against the spread of COVID-19 through droplets: A quantitative mechanistic study. *Extrem Mech Lett*. 2020;40:100924.
25. Qian Y, Willeke K, Grinshpun SA, Donnelly J, Coffey CC. Performance of N95 respirators: filtration efficiency for airborne microbial and inert particles. *Am Ind Hyg Assoc J*. 1998;59:128–32.
26. Schilling K, Gentner D, Wilen L, Medina A, Buehler C, Perez-Lorenzo LJ, et al. An accessible method for screening aerosol filtration identifies poor-performing commercial masks and respirators. *J Exposure Sci Environ Epidemiol*. 2020;31:943–52.
27. Prince SE, Chen H, Tong H, Berntsen J, Masood S, Zeman KL, et al. Assessing the effect of beard hair lengths on face masks used as personal protective equipment during the COVID-19 pandemic. *J Exposure Sci Environ Epidemiol*. 2021;18:1–8.
28. Shakya KM, Noyes A, Kallin R, Peltier RE. Evaluating the efficacy of cloth face-masks in reducing particulate matter exposure. *J Exposure Sci Environ Epidemiol*. 2017;27:352–7.
29. Darby S, Chulliyallipalil K, Przyjalowski M, McGowan P, Jeffers S, Giltinan A, et al. COVID-19: mask efficacy is dependent on both fabric and fit. *Future Microbiol*. 2021;16:5–11.
30. Verma S, Dhanak M, Frankenfield J. Visualizing the effectiveness of face masks in obstructing respiratory jets. *Phys Fluids*. 2020;32:061708.
31. Hui DS, Chow BK, Chu L, Ng SS, Lee N, Gin T, et al. Exhaled air dispersion during coughing with and without wearing a surgical or N95 mask. *PLoS One*. 2012;7:1–7.
32. Tang JW, Liebner TJ, Craven BA, Settles GS. A Schlieren optical study of the human cough with and without wearing masks for aerosol infection control. *J R Soc Interface*. 2009;6:S727–S736.
33. Mittal R, Ni R, Seo JH. The flow physics of COVID-19. *J Fluid Mech*. 2020;894:F2.
34. Solano T, Mittal R, Shoele K. One size fits all? A simulation framework for face-mask fit on population-based faces. *PLoS One*. 2021;16:1–23.
35. Liu S, Novoselac A. Transport of airborne particles from an unobstructed cough jet. *Aerosol Sci Technol*. 2014;48:1183–94.
36. Shadden SC, Dabiri JO, Marsden JE. Lagrangian analysis of fluid transport in empirical vortex ring flows. *Phys Fluids*. 2006;18:047105.
37. Peng J, Dabiri JO. Transport of inertial particles by Lagrangian coherent structures: application to predator–prey interaction in jellyfish feeding. *J Fluid Mech*. 2009;623:75–84.
38. Dabiri JO. California Institute of Technology; 2021. <https://dabirilab.com/software>.
39. Fuchs R, Schindler B, Peikert R In: Peikert R, Hauser H, Carr H, Fuchs R, editors. Scale-space approaches to FTLE ridges; in: *Topological Methods in Data Analysis and Visualization II*. Berlin, Heidelberg: Springer Berlin Heidelberg; 2012. p. 283–96.
40. Green MH, Curet OM, Patankar NA, Hale ME. Fluid dynamics of the larval zebrafish pectoral fin and the role of fin bending in fluid transport. *Bioinspiration Biomim*. 2012;8:016002.
41. Sangras R, Kwon OC, Faeth GM. Self-preserving properties of unsteady round nonbuoyant turbulent starting jets and puffs in still fluids. *J Heat Transf*. 2002;124:460–9.
42. O'Kelly E, Arora A, Pirog S, Ward J, Clarkson PJ. Comparing the fit of N95, KN95, surgical, and cloth face masks and assessing the accuracy of fit checking. *PLoS One*. 2021;16:1–14.

ACKNOWLEDGEMENTS

The authors would like to acknowledge the assistance of the members of the Applied Fluid Research Group in the Department of Aerospace Engineering at Auburn University.

AUTHOR CONTRIBUTIONS

All authors contributed to the design and conceptualization of the study. SM and WM designed and fabricated the experimental setup, and conducted the experiments. SM and WM analyzed the data in discussions with JC and VR. SM and WM composed the first draft of the manuscript. All authors edited the manuscript and provided critical feedback on finalizing the manuscript. VR and JC were also responsible for obtaining funding to carry out this work.

FUNDING

This material is based upon work supported by the National Science Foundation under Grant nos. 2035488 and 2035489, monitored by Dr. Ronald Joslin.

COMPETING INTERESTS

The authors declare no competing interests.

ADDITIONAL INFORMATION

Correspondence and requests for materials should be addressed to Sarah Morris or Vrishank Raghav.

Reprints and permission information is available at <http://www.nature.com/reprints>

Publisher's note Springer Nature remains neutral with regard to jurisdictional claims in published maps and institutional affiliations.